PHYSICAL PROPERTIES OF SPECTROSCOPICALLY-CONFIRMED GALAXIES AT $Z \gtrsim 6$. II. MORPHOLOGY OF THE REST-FRAME UV CONTINUUM AND LYMAN-α EMISSION[*]

Linhua Jiang[1,2,3], Eiichi Egami[2], Xiaohui Fan[2], Rogier A. Windhorst[1], Seth H. Cohen[1], Romeel Davé[2,4], Kristian Finlator[5], Nobunari Kashikawa[6], Matthew Mechtley[1], Masami Ouchi[7,8], and Kazuhiro Shimasaku[9]

Draft version March 4, 2013

ABSTRACT

We present a detailed structural and morphological study of a large sample of spectroscopically-confirmed galaxies at $z \gtrsim 6$, using deep *HST* near-IR broad-band images and Subaru optical narrow-band images. The galaxy sample consists of 51 Lyα emitters (LAEs) at $z \simeq 5.7$, 6.5, and 7.0, and 16 Lyman-break galaxies (LBGs) at $5.9 \lesssim z \lesssim 6.5$. These galaxies exhibit a wide range of rest-frame UV continuum morphology in the *HST* images, from compact features to multiple component systems. The fraction of merging/interacting galaxies reaches $40 - 50\%$ at $M_{1500} \lesssim -20.5$ mag, suggesting hierarchical build-up of the brightest galaxies at high redshift. We use half-light radius to describe the galaxy sizes, and find that the intrinsic radii $r_{\rm hl,in}$, after correction for PSF broadening, are roughly between $r_{\rm hl,in} \simeq 0\overset{''}{.}05$ and $0\overset{''}{.}3$, with a median value of $0\overset{''}{.}13$ ($\sim$0.75 kpc). This is consistent with the sizes of bright LAEs and LBGs at $z \gtrsim 6$ in previous studies. In addition, more luminous galaxies tend to have larger physical sizes, exhibiting a size-luminosity relation $r_{\rm hl,in} \propto L^{0.2}$. The slope 0.2 is significantly flatter than those in previous fainter LBG samples. We for the first time characterize the morphology of $z \geq 6$ galaxies using nonparametric methods, including the CAS system, the Gini and M_{20} parameters. Compared to low-redshift galaxies, our galaxies appear in slightly different locations in the parameter space, mainly due to their small sizes in the *HST* images. However, we find strong correlations between the measured parameters, as expected from their definitions. This implies that these nonparametric methods could be still applicable for $z \geq 6$ galaxies, if used with caution. We search for extended Lyα emission halos around LAEs at $z \simeq 5.7$ and 6.5, by stacking a number of narrow-band images. We do not find evidence of extended halos predicted by cosmological simulations. Such Lyα halos, if exist, could be weaker than predicted. Finally, we investigate any positional misalignment between UV continuum and Lyα emission in LAEs. While the two positions are generally consistent, several merging galaxies show significant positional differences. It is likely caused by disturbed ISM distribution due to merging activity.

Subject headings: cosmology: observations — galaxies: evolution — galaxies: high-redshift

1. INTRODUCTION

[1] School of Earth and Space Exploration, Arizona State University, Tempe, AZ 85287-1504, USA; linhua.jiang@asu.edu
[2] Steward Observatory, University of Arizona, 933 North Cherry Avenue, Tucson, AZ 85721, USA
[3] Hubble Fellow
[4] Physics Department, University of the Western Cape, 7535 Bellville, Cape Town, South Africa
[5] DARK fellow, Dark Cosmology Centre, Niels Bohr Institute, University of Copenhagen
[6] Optical and Infrared Astronomy Division, National Astronomical Observatory, Mitaka, Tokyo 181-8588, Japan
[7] Institute for Cosmic Ray Research, The University of Tokyo, 5-1-5 Kashiwanoha, Kashiwa, Chiba 277-8582, Japan
[8] Kavli Institute for the Physics and Mathematics of the Universe, The University of Tokyo, 5-1-5 Kashiwanoha, Kashiwa, Chiba 277-8583, Japan
[9] Department of Astronomy, University of Tokyo, Hongo, Tokyo 113-0033, Japan

Galaxy structural and morphological studies provide basic apparent information about galaxies. Nearby galaxies are generally classified into three broad categories, spiral, elliptical, and irregular galaxies. The majority of luminous nearby galaxies ($z \lesssim 0.1$) are spirals and ellipticals (Abraham & van den Bergh 2001). At higher redshift, galaxies are less well developed, and the fraction of irregular galaxies increases steadily (e.g., Driver et al. 1995, 1998). In the redshift range of $0.1 \lesssim z \lesssim 1$, galaxy morphology and structure have been well studied (e.g., Brinchmann et al. 1998; Lilly et al. 1998; Schade et al. 1999; Carlberg et al. 2000; Le Fèvre et al. 2000; van den Bergh et al. 2000, and references therein). These galaxies show more disturbed structures than nearby galaxies do in the rest-frame UV and optical (e.g., Abraham & van den Bergh 2001; Windhorst et al. 2002; Taylor-Mager et al. 2007; Blanton & Moustakas 2009; Shi et al. 2009). The fraction of irregular galaxies increases from less than 10% at $z \lesssim 0.5$ to $\sim$ 30% at $z \simeq 1$ (e.g., Brinchmann et al. 1998; van den Bergh et al. 2000). In addition, more galaxies were identified as merging systems, reflecting hierarchical build-up of galaxies and mass assembly in cold dark matter (CDM) scenario (White & Rees 1978; Cole et al. 2000). For example, nearly 20% of $z \simeq 1$ galaxies in the Le Fèvre et al. (2000) sample are in close pairs.

For galaxies at $z \gtrsim 2 - 3$, morphological classifica-

tion is challenging, as most galaxies appear peculiar. Galaxies are also smaller towards higher redshift (Ferguson et al. 2004). In addition, galaxies appear much fainter due to the cosmological $(1 + z)^4$ surface brightness dimming. Traditional classifications, including Hubble's tuning-fork system, do not work any more. Therefore, nonparametric methods such as the CAS system (Conselice 2003) and the Gini and M_{20} parameters (Lotz et al. 2004) play an important role. Most morphological and structural analyses in this redshift range were done in the GOODS fields (Giavalisco et al. 2004), because of the high-quality $Hubble Space Telescope$ (HST) data (e.g., Lowenthal et al. 1997; Ravindranath et al. 2006; Law et al. 2007; Cassata et al. 2010). In the rest-frame UV, $z \geq 3$ galaxies are usually compact (from one to several kpc), but many of them display extended features or multiple clumps in deep HST images (e.g., Giavalisco et al. 1996; Venemans et al. 2005; Ravindranath et al. 2006; Pirzkal et al. 2007; Conselice & Arnold 2009; Gronwall et al. 2011; Law et al. 2012). For example, the Ravindranath et al. (2006) sample contains thousands of photometrically-selected (hereafter photo-selected) LBGs at $z \gtrsim 2.5$, and about 30% of them have multiple cores. In Law et al. (2012), a sample of spectroscopically-confirmed (hereafter spec-confirmed) galaxies also showed a high fraction of interacting systems.

In the highest-redshift range $z \gtrsim 6$, morphological studies become difficult. Galaxies appear very faint, and their rest-frame UV light moves to the near-IR wavelength range, where telescope resolution is poorer. A typical galaxy occupies only a few pixels even in HST near-IR images, so nonparametric parameters have not been determined for these galaxies, and size is usually the only physical parameter that can be reliably measured in the literature. Studies based on photo-selected galaxies have shown that $z \gtrsim 6$ galaxies are generally very compact, and most of them are just barely spatially resolved. For example, Oesch et al. (2010) reported the sizes of 16 LBGs at $z \geq 7$ in the Hubble Ultra-Deep Field (HUDF). They found that only two in their sample show extended features, and the rest are very compact (≤ 1 kpc). This sample is very faint. Observations of a handful brighter galaxies with spectroscopic redshifts also suggest compact morphology, with a typical size of $\lesssim 1$ kpc (e.g., Stanway et al. 2004; Dow-Hygelund et al. 2007; Cowie et al. 2011). Note that galaxy size is correlated with physical properties, such as mass and luminosity at low redshift. Such relations still exist in high-redshift galaxies, but could have evolved with time (e.g., Grazian et al. 2012; Mosleh et al. 2012).

In this paper, we will carry out a structural and morphological study of a sample of 67 spec-confirmed galaxies at $z \gtrsim 6$. The sample is the largest collection of spec-confirmed galaxies in this redshift range, including 51 Lyα emitters (LAEs) and 16 Lyman-break galaxies (LBGs). This paper is the second in a series presenting the physical properties of these galaxies. In the first paper of the series (Jiang et al. 2013, hereafter Paper I), we presented deep Subaru optical and HST near-IR data. We also derived various rest-frame UV continuum and Lyα emission properties, including UV-continuum

slope β, the Lyα rest-frame equivalent width (EW), and star formation rates (SFRs). These galaxies have steep UV continuum slopes roughly between $\beta \simeq -1.5$ and $\beta \simeq -3.5$, with a median value of $\beta \simeq -2.3$. They have a range of Lyα EW from $\sim$10 to $\sim$300 Å. Their SFRs are moderate from a few to a few tens solar masses per year. In this paper we will study the structure and morphology of their rest-frame UV-continuum emission based on our HST images, and of their Lyα emission based on our ground-based narrow-band images.

The layout of the paper is as follows. In Section 2, we briefly review our galaxy sample and the optical and near-IR data that will be used for the paper. We measure the structure and morphology of UV continuum emission in Section 3, and of the Lyα emission in Section 4. We then discuss our results and summarize the paper in Section 5. Throughout the paper we use a Λ-dominated flat cosmology with $H_0 = 70$ km s^{-1} Mpc^{-1}, $\Omega_m = 0.3$, and $\Omega_\Lambda = 0.7$ (Komatsu et al. 2011). All magnitudes are on the AB system (Oke & Gunn 1983).

2. GALAXY SAMPLE AND DATA

In Section 2 of Paper I we provided a detailed description of our galaxy sample, and the data that we used in multi-wavelength bands. Here we summarize this information below. There are a total of 67 spec-confirmed galaxies in our sample: 62 are from the Subaru Deep Field (SDF; Kashikawa et al. 2004), and the remaining 5 are from the Subaru XMM-Newton Deep Survey field (SXDS; Furusawa et al. 2008). They represent the most luminous galaxies in terms of Lyα luminosity (for LAEs) or UV continuum luminosity (for LBGs) in this redshift range. The SDF galaxy sample contains 22 LAEs at $z \simeq 5.7$ (Shimasaku et al. 2006; Kashikawa et al. 2011), 25 LAEs at $z \simeq 6.5$ (Taniguchi et al. 2005; Kashikawa et al. 2006, 2011), and a LAE at $z = 6.96$ (Iye et al. 2006). The LAEs at $z \simeq 5.7$ and 6.5 have a relatively uniform magnitude limit of 26 mag in the narrow bands NB816 and NB921, and thus make a well-defined sample. The SDF sample also contains 14 LBGs at $5.9 \lesssim z \lesssim 6.5$ (Nagao et al. 2004, 2005, 2007; Ota et al. 2008; Jiang et al. 2011; Toshikawa et al. 2012). These LBGs were selected with different criteria, and have a rather inhomogeneous depth. The SXDS sample consists of 5 galaxies, including 2 LBGs at $z \simeq 6$ (Curtis-Lake et al. 2012) and 3 LAEs at $z \simeq 6.5$ (Ouchi et al. 2010). In Table 1 of Paper I, we summarized all the observed data of these galaxies.

The SDF and SXDS were observed with Subaru Suprime-Cam (Kashikawa et al. 2004; Furusawa et al. 2008). They have extremely deep optical images in a series of broad and narrow bands. Public stacked images are also available for the two fields, but the public data do not include the images taken recently. In Paper I, we produced our own stacked images in six broad bands ($BVRi'z'y$) and three narrow bands (NB816, NB921, and NB973) by including all available data in the archive. Our stacked images have great depth with excellent PSF full width at half maximum (FWHM) of $0.\!''5 - 0.\!''7$. The near-IR imaging data for the SDF galaxies are from three HST GO programs 11149 (PI: E. Egami), 12329 and 12616 (PI: L. Jiang). The HST observations were made with a mix of instruments and depth. The majority of the galaxies were observed with WFC3 in the F125W (here-

after J_{125}) and F160W (hereafter H or H_{160}) bands. The typical integration time was two HST orbits (roughly 5400 sec) per band. This provides a depth of ~ 27.5 mag (5σ detection) in the J_{125} band and ~ 27.1 mag in the H_{160} band (see also Windhorst et al. 2011). The pixel size in the final reduced WFC3 images is $0.''06$. Several SDF galaxies were observed with NICMOS in the F110W (hereafter J_{110}) and H_{160} bands. The typical integration time was also two HST orbits. The depth in the two bands are ~ 26.4 mag and ~ 26.1 mag, respectively. The pixel size in the final reduced NICMOS images is $0.''1$. The five SXDS galaxies were covered by the UKIDSS Ultra-Deep Survey (UDS). Their HST WFC3 near-IR data were obtained from the Cosmic Assembly Near-infrared Deep Extragalactic Legacy Survey (CANDELS; Grogin et al. 2011). The exposure depth of the CANDELS UDS data is 1900 sec in the J_{125} band and 3300 sec in the H_{160} band.

The majority of the galaxies in our sample were detected with high significance in the near-IR images. Only 15 of them — among the faintest in the optical — have weak detections ($< 5\sigma$) in the J band (J_{125} or J_{110}). In Table 1 of Paper I we listed the optical and near-IR photometry of the galaxies. In Table 2 of Paper I we presented basic physical properties, including the rest-frame UV continuum luminosity and slope β, the Lyα luminosity and EW, and their SFRs, etc. The thumbnail images of all the galaxies are provided in Appendix A of Paper I.

3. UV CONTINUUM MORPHOLOGY

In this section we will derive structural and morphological parameters for the galaxies in our sample. Although our galaxies represent the most luminous galaxies at $z \gtrsim 6$, they appear faint and small compared to lower-redshift galaxies. The majority of them are point-like sources in the optical images. Even in the HST WFC3 images they usually occupy a very limited number of pixels. Hence, the study of these distant galaxies is challenging. In previous literature, galaxy size was often the only parameter that could be reliably measured for $z \gtrsim 6$ galaxies. Classifications for nearby galaxies, such as the classical Hubble's tuning-fork system, cannot be applied to these objects. In this section, we will measure the sizes of our galaxies, and try to characterize their morphology using nonparametric methods, such as the CAS system (Conselice 2003) and the Gini and M_{20} parameters (Lotz et al. 2004). These methods are primarily used for low-redshift galaxies, though they have already been used for galaxies at $z = 4 \sim 6$ (e.g., Pirzkal et al. 2007; Conselice & Arnold 2009). We will also study interacting/merging systems in our sample.

In order to calculate the above parameters, we take advantage of all our HST images. For each galaxy in our sample, we combine (the weighted average) its J- and H-band images and make a stacked HST image to improve the signal-to-noise (S/N) ratio. By doing this we assume that the effect of the morphological k-correction — the dependence of galaxy structure on wavelength — is negligible in the wavelength range considered (Windhorst et al. 2002). This is because the J and H bands cover a similar rest-frame UV wavelength range (~ 1780 Å vs. ~ 2200 Å) for $z \simeq 6$ galaxies. Our further analyses are then based on the stacked images.

The J and H bands do not cover Lyα emission for our galaxies, so the morphology in the stacked images is purely from their UV continuum emission (other nebular lines can be safely ignored in general; see also Cai et al. 2011 and Kashikawa et al. 2012). In Figure 1, we show the thumbnail images of 47 (out of 67) galaxies that have more than 8σ detections of their total fluxes in the stacked images. We will focus on these 47 galaxies in this section. Table 1 lists the 47 galaxies. Columns 1 to 4 list the galaxy number, coordinates, and redshift, directly taken from Paper I. Note that we exclude object no. 12, since it overlaps with a bright foreground star, as explained in Paper I.

We do not show in Figure 1 the galaxies (19 out of 67) that have $< 8\sigma$ detections, as we would not obtain reliable structural and morphological information with such low S/N ratios. Instead, we combine their images, and make a stacked image for these 19 faint galaxies. The individual images are scaled before stacking, so that the galaxies all have the same magnitude. Because of the scaling, the individual weight images have different sky noise. The final stacked image has a much higher S/N ratio.

3.1. Size

We use the half-light radius $r_{\rm hl}$ to describe the size of a galaxy. The half-light radius $r_{\rm hl}$ is a radius enclosing a half of the total light. The total light is measured within a radius of $1.5\,r_{\rm P}$, where $r_{\rm P}$ is the Petrosian radius, at which the surface brightness (SB) is 20% of the average SB within this radius. The factors 1.5 and 20% are chosen to match those in previous studies of high-redshift galaxies (e.g. Lotz et al. 2006; Conselice & Arnold 2009). The Petrosian radii $r_{\rm P}$ for the majority of the 47 galaxies in our sample are between $0.''3$ and $0.''7$, consistent with the radius range $0.''2 \sim 0.''6$ in the $z \simeq 4-6$ LBG samples of Conselice & Arnold (2009).

Column 5 in Table 1 lists the observed $r_{\rm hl}$ calculated using `SExtractor` (Bertin & Arnouts 1996). The upper panel of Figure 2 shows $r_{\rm hl}$ as the function of M_{1500}, the absolute AB magnitude of the continuum at rest-frame 1500 Å. Physical quantities such as M_{1500} were derived in Paper I. The blue and red circles in Figure 2 represent the LAEs at $z \simeq 5.7$ and 6.5 (including $z \simeq 7$), respectively, and the green circles represent the LBGs at $z \simeq 6$. These galaxies span a range of $r_{\rm hl}$ from $0.''1$ to $\sim 0.''28$, or 0.6–1.6 kpc, without correction for PSF broadening. The median value of the measured $r_{\rm hl}$ is $0.''17$ (~ 1 kpc). The stacked image of faint galaxies, shown as a star in Figure 2, has a relatively smaller radius $r_{\rm hl} \simeq 0.''14$. The median value of $r_{\rm hl}$ for the whole sample is $0.''16$.

We correct for PSF broadening and estimate intrinsic half-light radius $r_{\rm hl,in}$ in quadrature, i.e., $r_{\rm hl,in}^2 = r_{\rm hl}^2 - r_{\rm PSF}^2$, where $r_{\rm PSF}$ is the radius of the instrumental PSF, and is $0.''10$ in our HST WFC3 images. The above equation is a good approximation, if the PSF profile and the intrinsic object profile are Gaussian-like or other simple symmetric profiles. As we will see, some galaxies in our sample show rather asymmetric and extended features. These galaxies usually have sizes much larger than the PSF, so their measured $r_{\rm hl}$ are close to $r_{\rm hl,in}$. With this correction, the intrinsic half-light radii $r_{\rm hl,in}$ range from $\leq 0.''05$ (< 0.3 kpc) to $\sim 0.''26$ (~ 1.5

kpc), with a median value of $0\rlap{.}''14$ (~ 0.8 kpc). The $r_{\rm hl,in}$ in the stacked image of 19 faint galaxies is about $0\rlap{.}''1$. The median value of $r_{\rm hl,in}$ for the whole sample is $0\rlap{.}''13$ (~ 0.8 kpc). The results are plotted in the lower panel of Figure 2.

The galaxy sizes in our sample roughly agree with those of high-redshift LAEs and LBGs with similar luminosities in the previous literature. For example, Pirzkal et al. (2007) found that the average $r_{\rm hl}$ for a sample of luminous LAEs at $z \sim 5$ is $0\rlap{.}''17$. Taniguchi et al. (2009) found a median $r_{\rm hl}$ of $0\rlap{.}''15$ for LAEs at $z \sim 5.7$. In the Hathi et al. (2008) and Conselice & Arnold (2009) LBG samples of $z = 4 \sim 6$ galaxies, the $r_{\rm hl}$ range is $0\rlap{.}''1 \sim 0\rlap{.}''3$, similar to the $r_{\rm hl}$ range in our sample. Previous studies have shown that the galaxy size roughly scales with redshift as $(1+z)^{-m}$, with m close to 1.1–1.2 (e.g. Ferguson et al. 2004; Bouwens et al. 2006; Oesch et al. 2010; Mosleh et al. 2012), so the size of galaxies evolves slowly at high redshift. This is the reason that high-redshift galaxies have a similar size range. Malhotra et al. (2012) found, however, that LAEs have a roughly constant size in the redshift range of $2.25 < z < 6$, and do not show a size-redshift relation. While our sample does not have a large redshift coverage, our galaxy sizes are well consistent with those in their sample.

3.1.1. *Size-luminosity relation*

Figure 2 shows that brighter objects tend to have larger $r_{\rm hl}$, meaning that more luminous galaxies have larger physical sizes. This size-luminosity relation has been found in both low-redshift and high-redshift star-forming galaxies (e.g., Taniguchi et al. 2009; Oesch et al. 2010; Grazian et al. 2012; Ono et al. 2012). For example, with a large sample photo-selected LBGs at $z \sim 7$ in the CANDELS fields, Grazian et al. (2012) found a well-defined relation, $r_{\rm hl} \propto L^{1/2}$. We illustrate the size-luminosity relation in our sample by displaying the best log-linear fit in Figure 2 (dashed lines). The best fitting results in the two panels are $r_{\rm hl} \propto L^{0.14}$ and $r_{\rm hl,in} \propto L^{0.2}$, respectively. Although the relation is obvious, the slopes are not as steep as that in Grazian et al. (2012). The reason is that our galaxy sample is brighter. Our relation is derived from galaxies in the luminosity range of $M_{1500} \leq -19.5$ mag, while the Grazian et al. (2012) sample covers a range of $M_{\rm UV} \leq -18$ mag. Their relation largely depends on the galaxies fainter than –19.5 mag, as seen in Figure 9 of their paper. In the brighter galaxies, $r_{\rm hl}$ (or $r_{\rm hl,in}$) shows less of a trend with luminosity, as also pointed out by Grazian et al. (2012). In fact, for the most luminous galaxies with $M_{1500} \lesssim -21$ mag, their size shows little correlation with luminosity in our sample. These galaxies have likely reached a relatively mature structure even at $z \simeq 6$.

It should be pointed out that the size-luminosity relation is not significantly affected by our size measurements, i.e., we may lose more light at the edge of fainter galaxies, so that fainter galaxies tend to be smaller. This is because we only used high S/N detections ($> 8\sigma$). Previous simulations and deep HST observations have shown that the above effect is minor for high S/N detections (e.g., Ravindranath et al. 2006; Oesch et al. 2010). Furthermore, the size-luminosity relation in our sample is

not caused by a selection effect, i.e., we may have missed some faint galaxies with large sizes. There are two reasons. One is that the galaxies were selected in optical images, they are bright in the optical broad bands (for LBGs) or narrow bands (for LAEs). The other one is that galaxies at the faint end tend to be very small, due to their hierarchical formation and evolution (Grazian et al. 2012; see also Windhorst et al. 2008 for detailed discussion). Also note that the exclusion of 19 faint galaxies in our sample does not introduce bias to our results of the size-luminosity relation. Our HST near-IR data have relatively uniform depth (two orbits per band per pointing), so the 8σ cut indeed puts a flux limit on M_{1500} in Figure 2, which does not affect our results in the bright region of $M_{1500} < -19.5$ mag.

3.2. *Nonparametric Measurements of Morphology*

In this subsection, we will characterize galaxy structure and morphology using nonparametric methods, including the CAS (Concentration, Asymmetry, and Smoothness) system (Conselice 2003), the Gini coefficient G, and the M_{20} (second-order moment of the brightest 20% of a galaxy) parameters (Lotz et al. 2004). These methods have been widely used for low-redshift galaxies. They usually provide reliable description of galaxy structure, and are able to distinguish different types of galaxies. To obtain accurate measurements of these quantities, two criteria are often required: high S/N ratios and large object sizes compared to the PSF size. For low-redshift galaxies, especially those in HST images, the sizes of galaxies are many times larger than PSF, so the two criteria are naturally met in deep HST images. At higher redshift, galaxies are fainter and smaller, so it is difficult to meet the two criteria, and these parameters become less reliable. For example, Conselice & Arnold (2009) tested the five parameters for galaxies at high redshift up to $z \simeq 6$. They found that S fails to well describe clumpiness, while most of them can be used with caution.

3.2.1. *CAS parameters*

Concentration (C) measures how compact the galaxy light profile is. We adopt the most recently and commonly used definition (e.g., Bershady et al. 2000; Conselice 2003):

$$C = 5 \log \left(\frac{r_{80}}{r_{20}} \right), \qquad (1)$$

where r_{80} and r_{20} are the radii that contain 80% and 20% of the total galaxy flux, respectively. Column 6 in Table 1 shows the individual measurements of C. Compared to low-redshift galaxies, our galaxies have a relatively narrow range of C between ~ 2 and ~ 3. In particular, there is a lack of a population with $C > 3$, or a lack of highly-concentrated galaxies. This is likely because the measurements of r_{80} and r_{20} are not robust, due to the relatively low spatial resolution of the HST images for $z \geq 6$ galaxies. The inner radius r_{20} is usually smaller the PSF size. In particular, for highly-concentrated galaxies, r_{20} could be smaller than one pixel and is thus likely overestimated, so C is underestimated. Nevertheless, the derived C values generally reflect galaxy concentrations, as we will see in subsection 3.2.3.

Asymmetry (A) measures how rotationally symmetric a galaxy is (Abraham et al. 1996; Conselice 2003). It is calculated by $A = A_{\text{galaxy}} - A_{\text{background}}$, or:

$$A = \frac{\Sigma|I - I_{180}|}{\Sigma|I|} - \frac{\Sigma|B - B_{180}|}{\Sigma|I|}. \qquad (2)$$

In the first term A_{galaxy}, I is the galaxy image and I_{180} is the image rotated by $180°$ about the galaxy center. The galaxy center is determined to minimize A_{galaxy}. The second term has the same meaning, except that it is for the sky background. A constant sky background has been subtracted from each galaxy image, so $A_{\text{background}}$ is equal to zero in Equation 2. Usually, A is measured within a radius of $1.5\,r_{\text{P}}$. For our galaxies, however, A is very sensitive to this radius due to the small sizes of the galaxies (or the small numbers of pixels occupied). We choose to measure A using the galaxy pixels assigned by segmentation maps given by SExtractor. Column 7 in Table 1 gives the results. Because of our different method to calculate A, we cannot directly compare our results with others. We will show later that this A may still provide a reliable measurement of galaxy asymmetry.

Smoothness (S) or clumpiness measures how clumpy a galaxy is (Conselice 2003). This parameter is sensitive to image resolution, and only works well for galaxies many times larger than the PSF size. Because our galaxies are either barely resolved or a few times the PSF size, we do not use S in this paper.

3.2.2. Gini and M_{20} parameters

The Gini coefficient (G) measures how even the galaxy light distribution is (Abraham et al. 2003; Lotz et al. 2004). It is calculated over the pixels belonging to the galaxy. We use the formula given by Lotz et al. (2004) to calculate G:

$$G = \frac{1}{|\bar{I}|n(n-1)} \sum_{i=1}^{n} (2i - n - 1)|I_i|, \qquad (3)$$

where $|I_i|$ is the absolute value of the ith pixel, and $|\bar{I}|$ is the average of the absolute values. Column 8 in Table 1 shows the measurements. Compared to low redshift galaxies, e.g., $z \simeq 4$ LBGs in the HUDF (Lotz et al. 2006), our galaxies have slightly lower Gini coefficients. This may suggest that their light distribution is relatively even. Given the limitation of G (e.g. Lisker 2008), an alternative explanation is that the image resolution is relatively poorer in our basically drizzled 2-orbit images, compared to the well sampled and drizzled HUDF ACS images. So it cannot resolve subtle structures of the galaxies.

The M_{20} parameter, or the second-order moment of the brightest 20% of the galaxy, is similar to the concentration C and measures how the galaxy light is concentrated (Lotz et al. 2004). It is also calculated over the pixels belonging to the galaxy. The second-order moment of a pixel is defined by:

$$M_i = I_i[(x_i - x_c)^2 + (y_i - y_c)^2], \qquad (4)$$

where (x_c, y_c) is the galaxy center and (x_i, y_i) is the pixel position. We rank the pixels with decreasing order of flux, and select the brightest pixels whose total flux is equal to 20% of the total galaxy flux. Then M_{20} is the total moment of the selected pixels normalized by the total moment of all the galaxy pixels:

$$M_{20} = \log\left(\frac{\sum_i M_i}{M_{\text{tot}}}\right), \text{ while } \sum_i I_i < 0.2 I_{\text{tot}}. \qquad (5)$$

The results are shown in Column 9 of Table 1. Compared to low-redshift galaxies, our galaxies have a relatively narrow range of M_{20}, and is lack of highly-concentrated (very low M_{20}) galaxies. This is just like parameter C, and is caused by the low resolution of the images. We will see below the correlation between M_{20} and C, as expected from their definitions.

3.2.3. Relations among the morphological parameters

As we mentioned earlier, the CAS system and the Gini and M_{20} parameters are primarily used for low-redshift galaxies, and have not been used for $z \gtrsim 6$ galaxies. We for the first time used these morphological parameters for our $z \gtrsim 6$ galaxies. Most of our galaxies indeed do not meet the two criteria required to use these methods, i.e., high S/N ratios and large galaxy sizes compared to the PSF size. Here we check the applicability of these parameters to $z \gtrsim 6$ galaxies. It is meaningless to perform direct comparisons with low-redshift galaxies, due to the much smaller galaxy sizes compared to the PSF in our images. The low resolution would systematically bias the morphological measurements. As we have seen in the above subsections, C and M_{20} were underestimated at least for highly-concentrated galaxies. This was also noticed by Lotz et al. (2006). Our galaxies have systematically lower G values compared to low-redshift galaxies, likely because our images cannot resolve subtle structures. In addition, the definitions of A is slightly different for that in the literature. Therefore, instead of making comparison with low-redshift galaxies, we check these parameters internally, as most of the parameters are expected to correlate with each other, and we have seen such correlations in low-redshift galaxies (e.g. Lotz et al. 2004, 2006; Conselice & Arnold 2009).

Figure 3 shows the relations among CA, G, M_{20}, and M_{1500} for the galaxies in our sample. Smoothness S was not calculated because of the reason explained in subsection 3.2.2. As expected, these parameters are correlated with each other: each parameter is correlated with one or more of the other parameters. There are several strong relations among them. The dashed lines in Figure 3 are the best linear fits to these relations, which are explained as follows. The moment M_{20} is correlated well with C, A, and G. Both M_{20} and C describe how the galaxy light is concentrated, and they are thus correlated by definition. The relations between M_{20} and A & G reflect that more concentrated galaxies have more rotationally symmetric profiles and more unevenly distributed light. The Gini coefficient G is correlated with C and A, in addition to M_{20}. Its relations with C and A indicate that galaxies with more concentrated or more rotationally symmetric profiles tend to have more unevenly distributed light. G is also correlated with M_{1500}. At higher luminosities, G has higher values. As we will see in the next section, many bright galaxies in our sample are interacting systems, and thus show significantly uneven light distributions.

In Figure 3 we see all expected correlations among

these morphological parameters. Asymmetry A is defined in a slightly different way, but it is still correlated with M_{20} and G, indicating that our modified definition is reliable. Although it has been pointed out that concentration C must been used with caution due to small galaxy sizes, C shows good relations with G and M_{20}, and thus could be still reliable in most cases. We will see in the next subsection that the corrections applied to the above parameters are even better (smaller scatter) for bright galaxies in our sample. Therefore, morphological parameters such as C, A, G, and M_{20} could be still applicable for $z \gtrsim 6$ galaxies, if used with caution.

3.3. *Interacting Systems*

One of the interesting morphological topics is to study interacting/merging systems, which traces hierarchical mass assembly in the CDM scenario. A close visual inspection of Figure 1 shows that some galaxies are clearly extended with interacting or multi-component features. At lower redshift, these systems can be identified by pair counts (e.g., Le Fèvre et al. 2000), the CAS system (e.g., Conselice 2003), or the G and M_{20} parameters (e.g., Lotz et al. 2008). Galaxies at $z \geq 6$ are faint and small, so it is difficult to properly distinguish regular and interacting/merging systems. Although we derived morphological parameters $CAGM_{20}$ in the above subsections, their ability to identify merging systems at $z \geq 6$ has never been examined. Therefore, we identify interacting/merging systems by visual inspection. Visual classification is the earliest way for galaxy classification, and in many cases is still the best way to identify merging systems at high redshift.

We consider the following two types of galaxies as candidate interacting/merging systems: 1) galaxies with two or more distinct cores; and 2) galaxies with extended/elongated features and/or long tails. We identify these systems in 25 relatively bright ($M_{1500} \leq -20.5$ mag) galaxies. For fainter galaxies, our images are not deep enough to properly identify all faint components or extended features due to low S/N ratios. Figures 4 and 5 show 12 galaxies that are identified as interacting systems with $M_{1500} \leq -20.5$ mag. Figure 4 shows 11 galaxies in the stacked images, and Figure 5 shows the $z = 6.96$ LAE (no. 62) in the two J bands. The red profiles are the SB contours of the rest-frame UV emission. Six of them clear show double or multiple clumps, including no. 4, 24, 34, 49, 62, and 67. They usually have one bright core and one or more fainter clumps. No. 62 and 67 are particularly interesting. No. 62 in Figure 5 has almost two identical components, and no. 67 has three widely-separated cores. More discussion is given in the next subsection. Another 3 galaxies, including no. 36, 58, and 61, do not clearly show multiple clumps, but have long tails like tidal tails seen in low-redshift merging galaxies. The rest of the 12 systems (no. 15, 44, and 47) do not show multiple components or tails, but they are rather extended and elongated. They could be in the end of the merging process.

We estimate the fraction of mergers among galaxies with $M_{1500} \leq -20.5$ mag. The fraction is 48%, or 36% if we exclude the three galaxies that do not show multiple components or tails. The fraction is even higher in the galaxies with $M_{1500} \lesssim -21$ mag. We have 18 galaxies in this magnitude range, and 10 of them are

mergers. The fraction of mergers is 56%, or 39% if we exclude the three galaxies mentioned above. This is consistent with the fractions in the brightest galaxies at low redshift of $z \simeq 2-3$. For example, the fraction of mergers in the $M_B < -21$ mag galaxy sample of Conselice (2003) is 40%–50%. The typical fraction in the brightest galaxies in the sample of Law et al. (2012) is also ~ 40%. The merger fraction in fainter galaxies is smaller, because merger systems consist of multiple components, and have stronger SFRs and UV emission. For the galaxies fainter than $M_{1500} \simeq -20.5$ mag in our sample, our images are deep enough to identify double-core systems with comparable emission. We find that these systems are very rare at $M_{1500} \simeq -20.5$ mag. Studies in deeper fields clearly indicate a low merger fraction in low-luminosity galaxies. For example, Oesch et al. (2010) presented the morphology of 16 $z \geq 7$ LBGs in the HUDF, and only found two galaxies with extended features.

3.3.1. *Notes on individual objects*

Galaxy no. 62. No. 62 is a $z = 6.964$ LAE. It is the first spec-confirmed LAE at $z \sim 7$ (Iye et al. 2006). Figure 5 shows that it has two similar components in the both J bands. We use the two-dimensional fitting algorithm `GALFIT` (Peng et al. 2002) to model the two components. Two Sérsic functions are fitted to the two components (two left-hand images in Figure 5) simultaneously. The middle images in Figure 5 show the best model fits, and the residuals are on the right-hand side. The two components in the both bands can be well described by the Sérsic function. The separation between the two cores is about $0\overset{''}{.}2$ (~ 1 kpc) (see also Cai et al. 2011).

Galaxy no. 67. No. 67 is a LAE at $z = 6.595$. It was discovered as a giant LAE by Ouchi et al. (2009). It is one of the brightest galaxies in terms of both Lyα luminosity and UV continuum luminosity. The most striking feature is the three well separated cores lined up. The central core is relatively weak. The brighter side cores are even resolved in our ground-based $z-$ and y-band images. The separate between the two side cores reaches $\simeq 1\overset{''}{.}2$, or 7 kpc. This is the largest separation we have seen at $z \geq 6$. This object also has strong emission in the IRAC bands, suggesting a large stellar mass of $\geq 10^{10} M_{\odot}$ (Ouchi et al. 2009).

3.3.2. *Morphology of interacting systems*

As we mentioned, the above interacting galaxies were identified with visual inspection. Morphological parameters were not used because the criteria of interacting systems at $z \geq 6$ are unclear. We check our interacting systems in the parameter space in Figure 6. Figure 6 is similar to Figure 4, but only plots the galaxies with $M_{1500} \leq -20.5$ mag in our sample. The red squares represent the interacting galaxies. It is clear in Figure 6 that the interacting galaxies are almost indistinguishable from the rest in the space of all parameters except A. Asymmetry A is the only effective parameter to identify interacting systems. The galaxies with the largest A in our sample are nearly all interacting systems. A is widely accepted as the most efficient way to identify mergers at low redshift (e.g. Conselice 2003; Conselice & Arnold 2009; Lotz et al. 2006, 2008; Law et al. 2012). The typical criterion for low-redshift mergers is $A \gtrsim 0.30 - 0.35$.

Although all the mergers in our sample have A values greater than 0.35, the criterion also includes a large number of regular galaxies. This is not a good criterion for our galaxy sample, because of the slightly different definition of A and the low spatial resolution of our images as we emphasized earlier. A better criterion in Figure 6 is probably $A \gtrsim 0.45$, which includes the majority of the mergers, but few of non-merging galaxies.

Another striking feature in Figure 6 is the much better correlations among the morphological parameters compared to Figure 4. The scatter in the relations is much smaller for these bright galaxies with $M_{1500} \leq -20.5$ mag. There are two explanations. One is that bright galaxies have higher S/N ratios and cover more pixels in the HST images, so their morphological measurements are more robust. The other one is that galaxies with different luminosities occupy slightly different parameter space, so a sample covering a smaller luminosity range shows a smaller scatter in Figure 6. The real reason is very likely the combination of the two. In any case, Figure 6 strengthens our earlier conclusion that morphological parameters $CAGM_{20}$ could be still applicable for $z \geq 6$ galaxies.

4. Lyα MORPHOLOGY

In this section we will study the Lyα morphology of LAEs using our ground-based narrow-band images. We will not measure structure and morphology for individual galaxies, since they are mostly point-like objects in the ground-based images. Although these images have excellent PSF sizes of $\sim 0\farcs5 - 0\farcs7$, the PSF sizes are still much larger those of the HST images. Therefore, we will focus on Lyα halos around LAEs, which could extend many arcsec from the objects. We will also compare the positions of Lyα emission with those of UV continuum emission, and find any possible positional difference between the two.

4.1. *Lyα Halos*

Because of the resonant scattering of Lyα photons by neutral hydrogen, Lyα emission could form large diffuse Lyα halos around high-redshift galaxies. Steidel et al. (2011) first found very extended Lyα halos in a sample of luminous galaxies at $2 < z < 3$. The galaxies were UV continuum-selected, but more than a half of them show net Lyα emission and $\sim 20\%$ have Lyα EW greater than 20 Å. They were able to find large Lyα emission halos (≥ 80 kpc) in the stacked images of all sub-samples of their galaxies. They further claimed that all LBGs would be classified as LAEs or Lyα blobs, if imaging data are deep enough to detect Lyα halos. Matsuda et al. (2012) confirmed the existence of extended Lyα halos around $z \simeq 3$ galaxies. They used more than 2000 LAEs at $z \simeq 3.1$, and grouped them into sub-samples based on luminosity and surface overdensity. They stacked narrow-band (Lyα) images for each sub-sample, and found that all stacked images show extended (> 60 kpc) Lyα emission halos. Recently Feldmeier et al. (2013) found that the existence of Lyα halos around LAEs is not convincing. They also used a large sample of a few hundred LAEs at $z \simeq 2.1$ and 3.1. They payed particular attention to systematic effects from large-radius PSF and large-scale flat fielding, etc. When these effects were taken into account, they did not find strong evidence of extended Lyα halos in the stacked narrow-band images at either redshift. They tried a few ways to reconcile the discrepancy between their results and the previous results, yet the reason of the discrepancy is still not clear.

Stacking of narrow-band images has not been done for $z \geq 6$ galaxies. On the other hand, cosmological simulations have predicted the existence of extended Lyα emission around $z \geq 6$ galaxies (e.g., Zheng et al. 2011; Dijkstra & Kramer 2012; Jeeson-Daniel et al. 2012). For example, by including the resonant scattering of Lyα photons in both circumgalactic media and intergalactic medium (IGM), Zheng et al. (2011) showed that the Lyα emitting halo in a high-redshift galaxy can extend up to 1 Mpc. They further pointed out that such halos could be detected by stacking 100 $z \simeq 5.7$ LAEs in 4-hr exposure narrow-band images in the SXDS. Here we combine the narrow-band (Lyα) images of LAEs at $z \simeq 5.7$ and 6.5.

In order to detect diffuse Lyα halos around LAEs, we make use of all the known (spec-confirmed) LAEs at $z \simeq 5.7$ and 6.5 in the SDF and SXDS fields from Kashikawa et al. (2011) and Ouchi et al. (2008, 2010). The narrow-band images were taken with the Subaru telescope. The total integration time in the NB816 and NB921 bands are 10 and 15 hr for the SDF (Kashikawa et al. 2004), and ~ 4 hr and ~ 10 hr (depth slightly varies among five pointings) for the SXDS (Ouchi et al. 2008, 2010). The data reduction of the SDF images were presented in Section 2 of Paper I. The reduction of the SXDS images were done in the same way. These narrow-band images have great depth with excellent PSF sizes of $0\farcs5 \sim 0\farcs7$. We reject a small number of galaxies that are either very faint or blended with nearby bright objects. The final sample contains 43 LAEs at $z \simeq 5.7$ and 40 LAEs at $z \simeq 6.5$.

To stack these images, we first cut image stamps for all individual objects. We then re-sample image stamps, so that the objects are in the centers of each image. After all other objects in the images are masked out, we co-add (average) the images with sigma-clipping (5σ rejection). Figure 7 shows the stacked narrow-band Lyα images at the two redshifts. We did not subtract away continuum images. As we showed in Paper I, our LAEs have Lyα EWs greater than 20 Å. The median EW value is 74 Å, so their narrow-band photometry is completely dominated by the Lyα emission. Subtracting continuum images would significantly increase the background noise. In the above procedure we did not scale the objects to the same magnitude either, since we do not know how the SB of the Lyα halos scales with the total Lyα flux in a LAE. We perform a series of tests by stacking the images in different ways, including image stacking with median, with objects scaled to the same magnitude, and with bright objects only. The results are all very similar to the images shown in Figure 7. Our stacked images of LAEs reach a depth of roughly $1.2 \times 10^{-19} \, \mathrm{erg \, s^{-1} \, cm^{-2} \, arcsec^{-2}}$ (1σ) in both bands (see also Figure 8). We should point out that this depth is shallower than what we predicted assuming that the noise goes down with the square root of the image number. The reason is that the input images are not purely blank images, whose noise is dominated by background Poisson noise. These images are extremely deep and crowded, so LAEs have many nearby

objects. Although we were able to mask out the bright pixels of the nearby objects, we could not remove the light outside these pixels that may extend many pixels away. When we combine many images, these nearby objects contribute significant unavoidable noise to the co-added images (e.g., Windhorst et al. 2008).

Figure 7 clearly shows that the stacked Lyα emission is compact at the both redshifts, and do not show very extended diffuse halos. As a reference, we also show in Figure 7 the stacked images of stars (point sources). The stars are chosen to be separated, bright, but not saturated, in the same narrow-band images. They are combined in the same way as we did for LAEs. Figure 8 shows the radial profiles of the stacked LAEs (solid lines with error bars) as well as the profiles of the stars (dotted lines). The Lyα profiles roughly follow the PSF profiles, and their SB reach zero at $r \geq 2''$. In the upper panel, the profile FWHM of the stacked $z \simeq 5.7$ LAE and star are $0''.49$ and $0''.62$, respectively. In the lower panel the two FWHM values are $0''.61$ for the $z \simeq 6.5$ LAE and $0''.77$ for the star. The LAE profiles are broader than the PSF sizes by $\sim 26\%$, and exhibit slightly longer tails than the PSF profiles do. This is simply because galaxies are not point sources, and indicates that the Lyα emission is resolved but not very extended. In the previous sections we show that our LAEs have a range of sizes in their rest-frame UV emission. Hathi et al. (2008) stacked broad-band HUDF images for $z \sim 4-6$ LBGs and found that the galaxy SB profiles are apparently broader than the PSF profiles. Finkelstein et al. (2011) found that two $z \simeq 4.4$ LAEs have large sizes in Lyα than in UV continuum. So the slightly broader Lyα SB profiles compared to the PSF are just the nature of galaxies, and are not likely caused by diffuse Lyα halos predicted or found in previous studies. The $z = 5.7$ profile seems to exhibit slightly more extended radius than its PSF profile. Given the 1σ limit of $\sim 1.2 \times 10^{-19}$ erg s^{-1} cm^{-2} arcsec^{-2}, its SB is still consistent with zero at $r \geq 2''$. Therefore, Figure 8 does not show convincing evidence of extended Lyα halos.

It is difficult to answer whether our stacked images are deep enough to detect Lyα halos if they do exist at the two redshifts. Our images are certainly deep enough to detect the LBG halos at $z \simeq 3$ reported by Steidel et al. (2011) and the LAE halos at $z \simeq 3.1$ in Matsuda et al. (2012). The depth to detect $z \geq 6$ LAE halos is observationally unknown. For cosmological simulations, Zheng et al. (2011) predicted Lyα halo sizes in $z = 5.7$ LAEs. They found two characteristic scales for the halos. The inner steeper one extends to $3'' - 4''$, and the outer flatter one extends to a few tens of arcsec. While our images are not deep enough to detect the outer halos, they are almost deep enough to detect the inner scale halos as seen in Figure 3 of Zheng et al. (2011), where the Lyα radial profiles are shown for LAEs in dark matter halos of $\sim 10^{11} M_\odot$. As pointed out by Zheng et al. (2011), the size of diffuse Lyα emission also depends on the mass of dark matter halo. If the average mass of the dark matter halos in our LAEs is smaller than $10^{11} M_\odot$, our current data may not be able to detect the diffuse Lyα emission.

It is also likely that the Lyα halos (if exist) have been diluted to a much lower level during the construction of the stacked images. The stacked images can properly recover Lyα halos only when halos are smoothly and symmetrically distributed around galaxies. If halos are highly asymmetric and/or clumpy, the emission of halos will be significantly diluted in average stacked images, and could totally disappear in median stacked images. From the observations of $z \sim 6$ quasars or cosmological simulations, we know that the distribution of IGM at $z \sim 6$ is inhomogeneous (e.g. Fan et al. 2006; Mesinger 2010). If the distribution of IGM affects the shape of Lyα halos (via resonant scattering), the distribution of Lyα halos is also likely asymmetric and clumpy.

Finally, it is possible that these LAEs do not have extended Lyα halos, or that their halo emission is not as strong as predicted by Zheng et al. (2011), especially when dust is taken into account (e.g. Finkelstein et al. 2011). Zheng et al. (2011) did not consider dust in their simulations. We know that high-redshift LAEs are not free of dust. In particular, the brightest galaxies may exhibit significant dust extinction, as implied by their UV colors (see Paper I). When Lyα photons are resonantly scattered by dusty neutral hydrogen, the Lyα emission is substantially reduced (Yajima et al. 2012). The reduction is more severe at larger distance from the object, because photons at larger distance need to pass through more dust before they escape. This process would significantly reduce the visibility of possible diffuse Lyα emission, and makes it much more difficult to detect it. A much larger sample of LAEs is needed to answer this question.

4.2. *Lyα-Continuum Misalignment*

The comparison between the positions of UV continuum and Lyα emission provides useful information on how Lyα photons escape from a galaxy. Lyα and UV continuum photons are usually come from the same star-forming regions, although Lyα photons are likely more sensitive to the regions with more recent star-forming activity. As we mentioned earlier, Lyα emission is complicated by resonant scattering and IGM absorption. So the observed position of Lyα emission could be different from the position of UV continuum emission. For example, a large positional difference has been found in a $z = 3.334$ galaxy (**?**). Due to the small sizes of high-redshift galaxies, current ground-based observations are not able to detect these positional differences. We rely on HST, which has observed a large number of high-redshift galaxies. HST observations were mostly made for rest-frame UV continuum emission, and there is usually no suitable HST narrow-band filters for Lyα emission. One example for the HST imaging of Lyα emission is the work of Finkelstein et al. (2011), who observed the Lyα emission of a small sample of $\simeq 4.4$ LAEs with a narrow-band filter. They did not find strong evidence of positional misalignment between UV and Lyα emission.

We use our large sample of LAEs to search for possible positional offsets between UV and Lyα emission at $z \simeq 5.7$ and 6.5. We use our HST images as UV continuum images and Subaru narrow-band images as Lyα images. As mentioned above, the narrow-band images have excellent PSF FWHM sizes around $0''.5 \sim 0''.7$. During the construction of the HST images (Paper I), we have matched the coordinates of the HST images to those of the optical images. To avoid any large-scale variation, we refine the coordinates of the HST images. For each LAE, we find 10–20 nearby objects that are relatively

bright and round. We then match the positions of the nearby objects in the two sets of images. The typical refinement is smaller than the size of one pixel ($0\rlap{.}''06$). The uncertainty in the object positions, derived from the distribution of the nearby objects, is about the size of 1–2 pixels. We plot the Lyα positions on top of the UV continuum positions. Figure 9 shows a few examples of bright galaxies. The red profiles are the contours of the UV emission SB, and the green crosses indicate the positions (and 1σ uncertainties) of the Lyα emission.

For the majority of the LAEs in our sample, the positions of the UV continuum and Lyα emission agree with each other. In particular, we do not find positional misalignment at a significance level of $> 2\sigma$ among almost all compact and round LAEs. Object no. 3 in Figure 9 is a typical example, in which the center of the Lyα emission is close to the center of the continuum emission. For the merging/interacting systems, however, we see significant positional differences. Figure 9 shows the examples of these systems. They exhibit a variety of Lyα positions relative to the peak positions[11] of the UV continuum emission: 1) Lyα positions close to the positions of the brightest components in the UV images, including galaxies no. 15, 47, and 61; 2) Lyα positions close to the positions of the fainter components or merger tails in the UV images, including no. 14, 44, and 58; 3) Lyα positions are somewhere between the positions of the bright and faint components, but closer to the bright components, including no. 4 and 49. No. 62 and 67 are again interesting. The Lyα position of no. 62 is roughly in the middle of the two similarly bright components. No. 67 does not show three distinct Lyα emission clumps, as its UV emission does. Instead, it shows a single bright Lyα emission core with some extended features. The Lyα center is not at any of the three UV clumps. It is between the left and central clumps, and slightly closer to the central one.

Our results suggest that in compact galaxies the observed location of Lyα emission does not deviate from its original position, while in merging/interacting systems, the observed Lyα location could be significantly different from its original position, without preferential positions of offsets. If the final location of Lyα emission is determined by the process of resonant scattering, our results can be explained by the interstellar medium (ISM) distribution (e.g. Finkelstein et al. 2011). In a non-disturbed galaxy, the ISM distribution is relatively symmetric around the object (not necessarily uniform, it could be clumpy). The random scattering of photons does not have preferred directions, so the observed location is still close to its original location. In an interacting system, the ISM is re-distributed by merging activity. The distribution of the disturbed ISM is therefore not symmetric any more. This results in an offset of the observed Lyα position.

This result could have an impact on spectroscopy of bright LBGs at $z \geq 6$ (e.g. Stark et al. 2011; Curtis-Lake et al. 2012). While most of the positional

---

[11] For an interacting galaxy, the position of its peak emission (as seen from the SB contour) could be very different from the position of the overall galaxy emission measured by, for example, fitting Gaussian to the marginal x,y distributions (used by IRAF DAOPHOT). Here our positions refer to the positions of peak emission.

offsets in our sample are smaller than $0\rlap{.}''2$, at least two are around $0\rlap{.}''3 - 0\rlap{.}''4$. If one uses a $\leq 1''$ slit to identify their Lyα emission lines, based on the positions of continuum emission, one could miss them due to the large offsets. However, glaxies with such large offsets are very rare, so this result will not largely reduce the success rate of identifying Lyα lines in LBGs.

5. DISCUSSION AND SUMMARY

The comparison in Section 3.1 shows that the sizes of our galaxies are consistent with those of bright $z \gtrsim 6$ LAEs and LBGs in previous studies. This disagrees with the claim of Dow-Hygelund et al. (2007) that LAEs are more compact than LBGs. This is likely because the Dow-Hygelund et al. (2007) sample is very small while LAEs have a large range of sizes. It is indeed difficult to make proper comparisons without a large sample, as the galaxy size depends on redshift and luminosity. Most of our galaxies are LAEs. Another large LAE sample is the $z \simeq 5.7$ LAE sample by Taniguchi et al. (2009), who observed a number of LAEs at $z \simeq 5.7$ with the *HST* ACS F814W filter. Although this filter includes Lyα emission, it is so wide that its emission is dominated by UV continuum. They found that the average intrinsic size of the sample is $0\rlap{.}''13$, the same as ours. Among many photo-selected LBG samples at $z \gtrsim 6$, a recent large sample is the sample of Grazian et al. (2012). This sample contains a number of bright (as well as faint), photo-selected LBGs at $z \sim 6 - 7$ in the CANDELS field. The sizes of these galaxies are well consistent with those of our galaxies at the same luminosities. Therefore, we conclude that LAEs and LBGs with similar luminosities have similar physical sizes.

In this paper (and Paper I), galaxies found by the narrow-band technique are defined as LAEs and those found by the dropout technique are defined as LBGs. As we discussed in Paper I, this classification only reflects the methodology that we apply to select galaxies. It does not mean that the two types of galaxies are intrinsically different. In Section 5.3 of Paper I, when we derived the UV continuum luminosity function of LAEs, we used another popular definition of LAEs based on the Lyα EW, i.e., a galaxy is a LAE if its Lyα EW is greater than 20 Å. With this definition, almost all the galaxies in our sample are LAEs. This definition is physically more meaningful, but observationally difficult, because one can easily obtain a flux-limited sample, not a EW-limited sample. We have 16 LBGs (former definition) in our sample. They are not typical LBGs. They are spec-confirmed, and thus only represent those with strong Lyα emission. In Paper I we found that our LAEs and LBGs are indistinguishable in many aspects of the Lyα and UV continuum properties. In this paper, we further found that these LAEs and LBGs have similar physical sizes and morphological parameters. This confirms one of our conclusions in Paper I that LAEs are a subset of LBGs with strong Lyα emission lines.

This paper is the second in a series presenting the physical properties of a large sample of spec-confirmed galaxies at $z \gtrsim 6$. The sample consists of 51 LAEs and 16 LBGs, and represents the most luminous galaxies in terms of Lyα luminosity (for LAEs) or UV continuum luminosity (for LBGs) in this redshift range. In Paper I we derived various properties of rest-frame UV con-

tinuum and Lyα emission. In this paper we have conducted a detailed structural and morphological study of the galaxies using deep HST near-IR images and Subaru narrow-band images. In order to measure the morphology of rest-frame UV continuum emission, we constructed a stacked HST image for each object by combining its J- and H-band images. UV morphology was then measured for those with $> 8\sigma$ detections in the stacked HST images. We used half-light radius $r_{\rm hl}$ to describe the sizes of galaxies. The observed sizes of our galaxies, without correction for PSF broadening, are between 0''.1 and 0''.3 (or 0.6–1.6 kpc), with a median value of 0''.16. The intrinsic sizes $r_{\rm hl,in}$ in our sample are from $\leq$ 0''.05 (< 0.3 kpc) to $\sim$ 0''.26 (~ 1.5 kpc), with a median value of 0''.13 ($\sim$0.75 kpc). These values are consistent with those of bright, photo-selected LBGs at similar redshifts. Additionally, more luminous galaxies tend to have larger sizes, exhibiting a size-luminosity relation $r_{\rm hl,in} \propto L^{0.2}$. The slope 0.2 is significantly flatter than those in fainter LBG samples. Our objects show a wide range of morphology in the HST images, including compact galaxies and double/multiple component systems. The brightest galaxies in the sample have a large fraction of merging/interacting systems. The fraction of mergers reaches $40 - 50\%$ at $M_{1500} < -20.5$ mag, suggesting hierarchical build-up of galaxies at high redshift.

We for the first time described the structure and morphology of $z \geq 6$ galaxies using nonparametric methods, including the CAS system, the Gini and M_{20} parameters. Compared to low-redshift galaxies, $z \geq 6$ galaxies appear faint and small in HST images, so they usually do not meet the criteria required by these nonparametric methods for low-redshift galaxies. Because of this reason, our galaxies are located in slightly different regions in the parameter space. However, we found strong correlations between these parameters, as expected from

their definitions. This suggests the nonparametric methods could be still applicable for $z \geq 6$ galaxies, if used with caution. We also found that Asymmetry A is the only effective parameter to identify merging systems.

We for the first time searched for Lyα emission halos around $z \gtrsim 6$ galaxies in narrow-band images. We combined a large number of narrow-band images for LAEs at $z \simeq 5.7$ and 6.5, respectively. The stacked images reached a depth of $\sim 1.2 \times 10^{-19}$ erg s^{-1} cm^{-2} arcsec^{-2} (1σ). We did not find evidence of extended diffuse Lyα emission as predicted by cosmological simulations. It is possible that our images are still not deep enough to detect Lyα emission halos, or that the Lyα halo emission has been diluted to a much lower level during the construction of the stacked images. It is also possible that the halo emission is not as strong as predicted. A much larger LAE sample is needed to solve this question. We also investigated positional differences between the rest-frame UV continuum emission and Lyα emission in LAEs, using the HST images and optical narrow-band images. While in compact LAEs the two positions are well consistent, in some merging galaxies show significant positional differences, with no preferred directions of offsets. It was explained by the distribution of the disturbed ISM.

Facilities: HST (NICMOS,WFC3), *Spitzer* (IRAC), *Subaru* (Suprime-Cam)

REFERENCES

Abraham, R. G., Tanvir, N. R., Santiago, B. X., et al. 1996, MNRAS, 279, L47
Abraham, R. G., & van den Bergh, S. 2001, Science, 293, 1273
Abraham, R. G., van den Bergh, S., & Nair, P. 2003, ApJ, 588, 218
Bershady, M. A., Jangren, A., & Conselice, C. J. 2000, AJ, 119, 2645
Bertin, E., & Arnouts, S. 1996, A&AS, 117, 393
Blanton, M. R., & Moustakas, J. 2009, ARA&A, 47, 159
Bouwens, R. J., Illingworth, G. D., Blakeslee, J. P., & Franx, M. 2006, ApJ, 653, 53
Brinchmann, J., Abraham, R., Schade, D., et al. 1998, ApJ, 499, 112
Cai, Z., Fan, X., Jiang, L., et al. 2011, ApJ, 736, L28
Carlberg, R. G., Cohen, J. G., Patton, D. R., et al. 2000, ApJ, 532, L1
Cassata, P., Giavalisco, M., Guo, Y., et al. 2010, ApJ, 714, L79
Cole, S., Lacey, C. G., Baugh, C. M., & Frenk, C. S. 2000, MNRAS, 319, 168
Conselice, C. J., 2003, ApJS, 147, 1
Conselice, C. J., & Arnold, J. 2009, MNRAS, 397, 208
Cowie, L. L., Hu, E. M., & Songaila, A. 2011, ApJ, 735, L38
Curtis-Lake, E., McLure, R. J., Pearce, H. J., et al. 2012, MNRAS, 422, 1425
Dijkstra, M., & Kramer, R. 2012, MNRAS, 424, 1672
Dow-Hygelund, C. C., Holden, B. P., Bouwens, R. J., et al. 2007, ApJ, 660, 47
Driver, S. P., Windhorst, R. A., Ostrander, E. J., et al. 1995, ApJ, 449, L23

Driver, S. P., Fernandez-Soto, A., Couch, W. J., et al. 1998, ApJ, 496, L93
Fan, X., Carilli, C. L., & Keating, B. 2006, ARA&A, 44, 415
Feldmeier, J., Hagen, A., Ciardullo, R., et al. 2013, arXiv:1301.0462
Ferguson, H. C., Dickinson, M., Giavalisco, M., et al. 2004, ApJ, 600, L107
Finkelstein, S. L., Cohen, S. H., Windhorst, R. A., et al. 2011, ApJ, 735, 5
Furusawa, H., Kosugi, G., Akiyama, M., et al. 2008, ApJS, 176, 1
Giavalisco, M., Steidel, C. C., & Macchetto, F. D. 1996, ApJ, 470, 189
Giavalisco, M., Ferguson, H. C., Koekemoer, A. M., et al. 2004, ApJ, 600, L93
Grazian, A., Castellano, M., Fontana, A., et al. 2012, A&A, 547, A51
Grogin, N. A., Kocevski, D. D., Faber, S. M., et al. 2011, ApJS, 197, 35
Gronwall, C., Bond, N. A., Ciardullo, R., et al. ApJ, 743, 9
Hathi, N. P., Jansen, R. A., Windhorst, R. A., et al. 2008, AJ, 135, 156
Iye, M., Ota, K., Kashikawa, N., et al. 2006, Nature, 443, 186
Jeeson-Daniel, A., Ciardi, B., Maio, U., et al. 2012, MNRAS, 424, 2193
Jiang, L., Egami, E., Kashikawa, N., et al. 2011, ApJ, 743, 65
Jiang, L., Egami, E., Mechtley, M., et al. 2013, ApJ, submitted
Kashikawa, N., Shimasaku, K., Yasuda, N., et al. 2004, PASJ, 56, 1011

Kashikawa, N., Shimasaku, K., Malkan, M. A., et al. 2006, ApJ, 648, 7

Kashikawa, N., Shimasaku, K., Matsuda, Y., et al. 2011, ApJ, 734, 119

Kashikawa, N., Nagao, T., Toshikawa, J., et al. 2012, ApJ, 761, 85

Komatsu, E., Smith, K. M., Dunkley, J., et al. 2011, ApJS, 192, 18

Law, D. R., Steidel, C. C., Erb, D. K., et al. 2007, ApJ, 656, 1

Law, D. R., Steidel, C. C., Shapley, A. E., et al. 2012, ApJ, 745, 85

Le Fèvre, O., Abraham, R., Lilly, S. J., et al. 2000, MNRAS, 311, 565

Lilly, S., Schade, D., Ellis, R., et al. 1998, ApJ, 500, 75

Lisker, T. 2008, ApJS, 179, 319

Lotz, J. M., Primack, J., & Madau, P. 2004, AJ, 128, 163

Lotz, J. M., Madau, P., Giavalisco, M., Primack, J., & Ferguson, H. C. 2006, ApJ, 636, 592

Lotz, J. M., Davis, M., Faber, S. M., et al. 2008, ApJ, 672, 177

Lowenthal, J. D., Koo, D. C., Guzman, R., et al. 1997, ApJ, 481, 673

Malhotra, S., Rhoads, J. E., Finkelstein, S. L., et al. 2012, ApJ, 750, L36

Matsuda, Y., Yamada, T., Hayashino, T., et al. 2012, MNRAS, 425, 878

Mesinger, A. 2010, MNRAS, 407, 1328

Mosleh, M., Williams, R. J., Franx, M., et al. 2012, ApJ, 756, L12

Nagao, T., Taniguchi, Y., Kashikawa, N., et al. 2004, ApJ, 613, L9

Nagao, T., Kashikawa, N., Malkan, M. A., et al. 2005, ApJ, 634, 142

Nagao, T., Murayama, T., Maiolino, R., et al. 2007, A&A, 468, 877

Oesch, P. A., Bouwens, R. J., Carollo, C. M., et al. 2010, ApJ, 709, L21

Oke, J. B., & Gunn, J. E. 1983, ApJ, 266, 713

Ono, Y., Ouchi, M., Curtis-Lake, E., et al. 2012, arXiv:1212.3869

Ouchi, M., et al. 2008, ApJS, 176, 301

Ouchi, M., Mobasher, B., Shimasaku, K., et al. 2009, ApJ, 706, 1136

Ouchi, M., Shimasaku, K., Furusawa, H., et al. 2010, ApJ, 723, 869

Ota, K., Kashikawa, N., Malkan, M. A., et al. 2008, arXiv:0804.3448

Peng, C. Y., Ho, L. C., Impey, C. D., & Rix, H.-W. 2002, AJ, 124, 266

Pirzkal, N., Malhotra, S., Rhoads, J. E., & Xu, C. 2007, ApJ, 667, 49

Rauch, M., Becker, G. D., Haehnelt, M. G., et al. 2011, MNRAS, 418, 1115

Ravindranath, S., Giavalisco, M., Ferguson, H. C., et al. 2006, ApJ, 652, 963

Schade, D., et al. 1999, ApJ, 525, 31

Shi, Y., Rieke, G., Lotz, J., & Perez-Gonzalez, P. G. 2009, ApJ, 697, 1764

Shimasaku, K., Kashikawa, N., Doi, M., et al. 2006, PASJ, 58, 313

Stanway, E. R., Glazebrook, K., Bunker, A. J., et al. 2004, ApJ, 604, L13

Stark, D. P., Ellis, R. S., & Ouchi, M. 2011, ApJ, 728, L2

Steidel, C. C., Bogosavljević, M., Shapley, A. E., et al. 2011, ApJ, 736, 160

Taniguchi, Y., Ajiki, M., Nagao, T., et al. 2005, PASJ, 57, 165

Taniguchi, Y., Murayama, T., Scoville, N. Z., et al. 2009, ApJ, 701, 915

Taylor-Mager, V. A., Conselice, C. J., Windhorst, R. A., & Jansen, R. A. 2007, ApJ, 659, 162

Toshikawa, J., Kashikawa, N., Ota, K., et al. 2012, ApJ, 750, 137

van den Bergh, S., Cohen, J. G., Hogg, D. W., & Blandford, R. 2000, AJ, 120, 2190

Venemans, B. P., Röttgering, H. J. A., Miley, G. K., et al. 2005, A&A, 431, 793

White, S. D. M., & Rees, M. J. 1978, MNRAS, 183, 341

Windhorst, R. A., Taylor, V. A., Jansen, R. A., et al. 2002, ApJS, 143, 113

Windhorst, R. A., Hathi, N. P., Cohen, S. H., et al. 2008, Advances in Space Research, 41, 1965

Windhorst, R. A., Cohen, S. H., Hathi, N. P., et al. 2011, ApJS, 193, 27

Yajima, H., Li, Y., Zhu, Q., & Abel, T. 2012, MNRAS, 424, 884

Zheng, Z., Cen, R., Weinberg, D., Trac, H., & Miralda-Escudé, J. 2011, ApJ, 739, 62

TABLE 1
MORPHOLOGICAL PARAMETERS OF THE GALAXIES

No.	R.A.	Decl.	Redshift	$r_{\rm hl}$ ($''$)	C	A	G	M_{20}
2	13:24:38.940	+27:13:40.95	5.654	0.136	2.59	0.24	0.44	−1.49
3	13:23:54.601	+27:24:12.72	5.665	0.152	2.79	0.30	0.58	−1.71
4	13:24:16.468	+27:19:07.65	5.671	0.256	2.36	0.52	0.36	−1.07
5	13:24:32.885	+27:30:08.82	5.681	0.219	2.60	0.56	0.41	−1.35
7	13:24:11.887	+27:41:31.81	5.691	0.147	2.08	0.44	0.41	−1.48
10	13:24:11.868	+27:19:48.23	5.696	0.168	2.13	0.58	0.36	−1.03
14	13:24:15.987	+27:16:11.05	5.705	0.270	2.38	0.42	0.25	−0.93
15	13:23:47.120	+27:24:13.82	5.710	0.209	2.56	0.37	0.57	−1.55
17	13:24:28.313	+27:30:12.17	5.716	0.135	2.53	0.44	0.44	−1.44
19	13:24:33.097	+27:29:38.58	5.718	0.172	2.50	0.48	0.43	−1.30
20	13:25:20.192	+27:18:42.27	5.724	0.179	2.68	0.51	0.55	−1.29
21	13:24:16.128	+27:44:11.62	5.738	0.152	2.16	0.38	0.39	−1.15
22	13:24:18.082	+27:16:38.93	5.743	0.159	2.52	0.44	0.39	−1.69
23	13:25:23.411	+27:17:01.34	5.922	0.166	2.35	0.33	0.53	−1.38
24	13:24:23.705	+27:33:24.82	6.002	0.232	2.10	0.57	0.43	−1.24
25	13:24:13.004	+27:41:45.80	6.032	0.262	2.37	0.49	0.42	−1.40
27	13:23:44.747	+27:24:26.81	6.040	0.169	2.55	0.34	0.47	−1.58
28	13:24:37.191	+27:35:02.36	6.042	0.185	2.30	0.38	0.41	−1.59
29	13:25:22.120	+27:35:46.87	6.049	0.113	2.59	0.35	0.51	−1.39
30	13:24:40.527	+27:13:57.91	6.062	0.173	2.31	0.35	0.45	−1.40
31	13:24:30.633	+27:29:34.61	6.112	0.178	2.30	0.30	0.43	−1.17
33	13:24:41.264	+27:26:49.09	6.269	0.201	2.53	0.60	0.39	−1.72
34	13:24:18.450	+27:16:32.56	6.315	0.269	2.37	0.47	0.53	−1.20
35	13:25:19.463	+27:18:28.51	6.332	0.128	2.64	0.39	0.55	−1.71
36	13:24:26.559	+27:15:59.72	6.482	0.222	2.45	0.58	0.48	−1.19
37	13:24:31.551	+27:15:08.72	6.508	0.165	2.85	0.37	0.34	−1.53
38	13:24:10.766	+27:19:03.95	6.519	0.104	2.03	0.44	0.41	−1.28
39	13:24:42.452	+27:24:23.35	6.534	0.148	2.43	0.43	0.41	−1.47
40	13:24:05.895	+27:18:37.72	6.534	0.168	3.00	0.41	0.38	−1.40
43	13:24:00.301	+27:32:37.95	6.542	0.154	2.18	0.32	0.48	−1.42
44	13:23:45.632	+27:17:00.53	6.543	0.184	2.27	0.40	0.45	−1.25
45	13:24:55.583	+27:39:20.89	6.544	0.137	2.32	0.50	0.36	−1.50
46	13:24:20.628	+27:16:40.47	6.545	0.203	2.37	0.39	0.41	−1.19
47	13:23:45.757	+27:32:51.30	6.547	0.228	2.91	0.37	0.60	−1.86
48	13:24:40.643	+27:36:06.94	6.548	0.171	2.74	0.44	0.37	−1.28
49	13:23:45.937	+27:25:18.06	6.548	0.127	2.30	0.76	0.44	−1.09
50	13:24:18.416	+27:33:44.97	6.550	0.142	2.66	0.34	0.44	−1.45
52	13:24:34.284	+27:40:56.32	6.554	0.131	2.38	0.46	0.44	−1.34
54	13:23:43.190	+27:24:52.04	6.556	0.196	2.25	0.44	0.35	−1.18
58	13:24:55.772	+27:40:15.31	6.583	0.233	2.57	0.54	0.44	−1.18
59	13:24:58.508	+27:39:12.92	6.585	0.208	2.86	0.46	0.40	−1.03
61	13:23:49.186	+27:32:11.39	6.599	0.183	2.10	0.49	0.38	−1.37
62	13:23:53.054	+27:16:30.75	6.964	0.179	2.25	0.29	0.57	−1.15
63	13:24:15.678	+27:30:57.79	6.023	0.144	2.36	0.25	0.50	−1.34
64	13:24:40.239	+27:25:53.11	6.116	0.141	2.44	0.36	0.51	−1.57
66	13:23:52.680	+27:16:21.76	6.575	0.173	2.34	0.45	0.34	−1.04
67	13:24:10.817	+27:19:28.08	6.595	0.155	2.17	0.60	0.40	−0.69

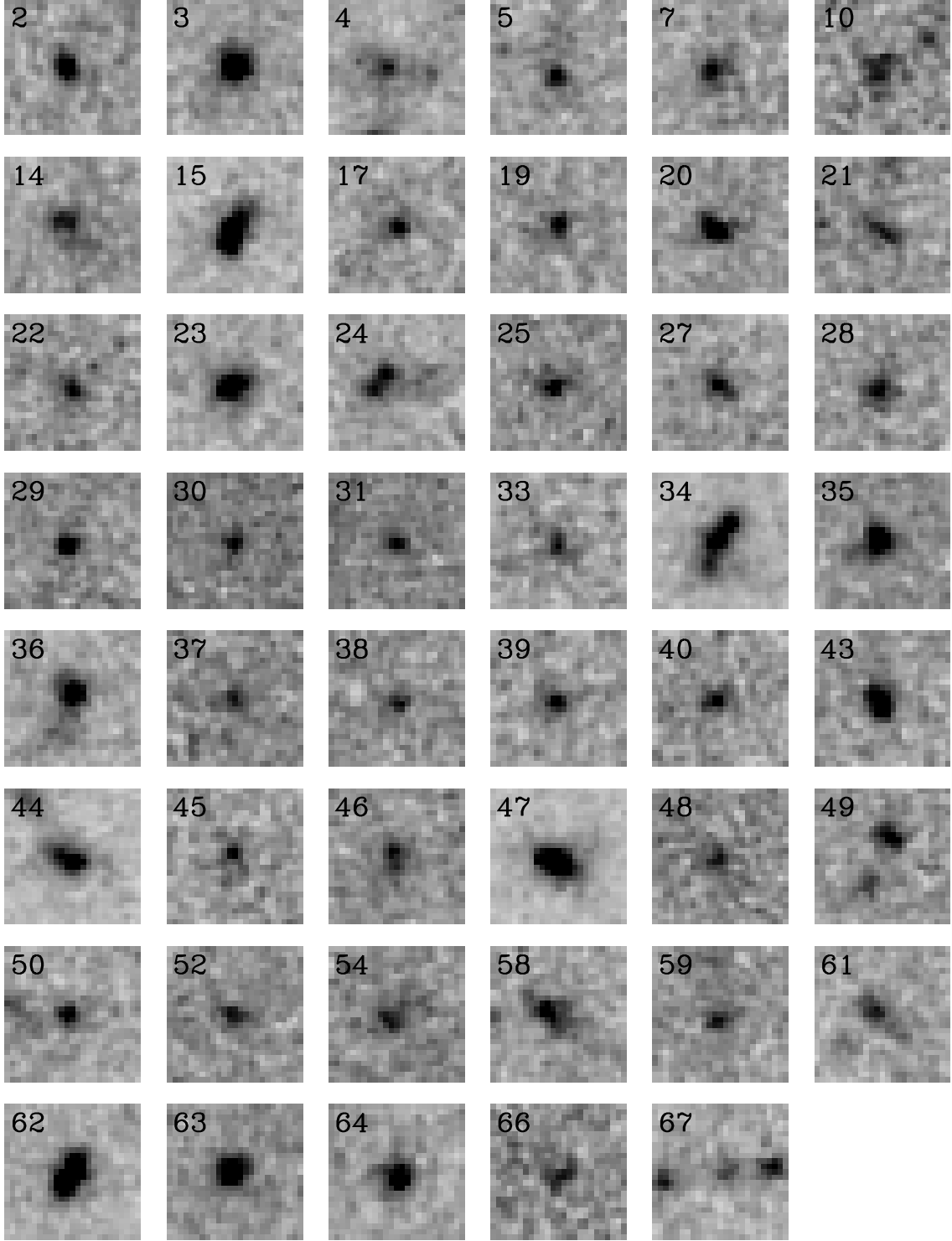NOTE. — The half-light radii $r_{\rm hl}$ are in units of arcsec.

FIG. 1.— Thumbnail images of the 47 (out of 67) galaxies that have more than 8σ detections in the stacked HST images, shown in order of increasing redshift. The image size is 25 pixel square, which corresponds to $2\rlap{.}''5 \times 2\rlap{.}''5$ in NICMOS images (no. 25, 30, and 31), or $1\rlap{.}''5 \times 1\rlap{.}''5$ in WFC3 images (the rest).
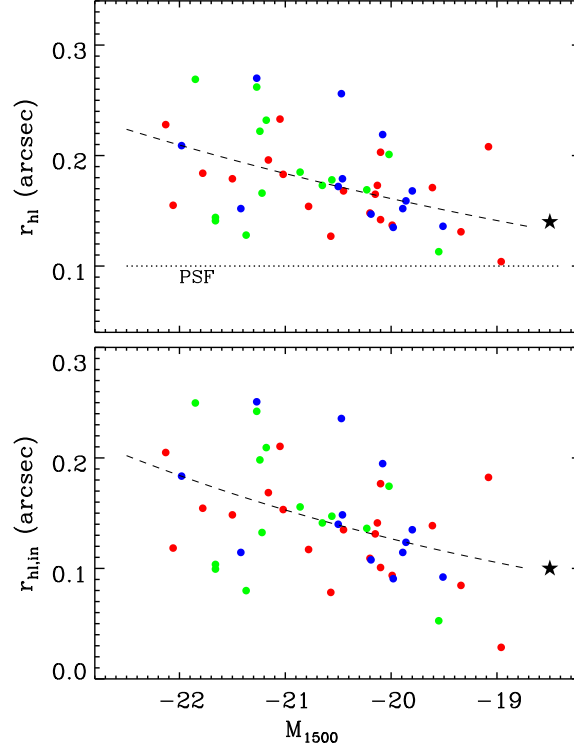
FIG. 2.— Half-light radius as a function UV continuum luminosity M_{1500}. The upper panel shows the observed radius $r_{\rm hl}$ without correction for PSF broadening. The dotted line indicates the PSF size in our *HST* WFC3 images. The lower panel shows the intrinsic radius $r_{\rm hl,in}$ after correction for PSF broadening. The blue and red circles represent the LAEs at $z \simeq 5.7$ and 6.5 (including $z \simeq 7$), respectively, and the green circles represent the LBGs at $z \simeq 6$. The star represents the stacked object of 19 faint galaxies. The dashed lines are the best log-linear fits to all the data points, suggesting a good size-luminosity relation: brighter objects tend to have larger physical sizes.
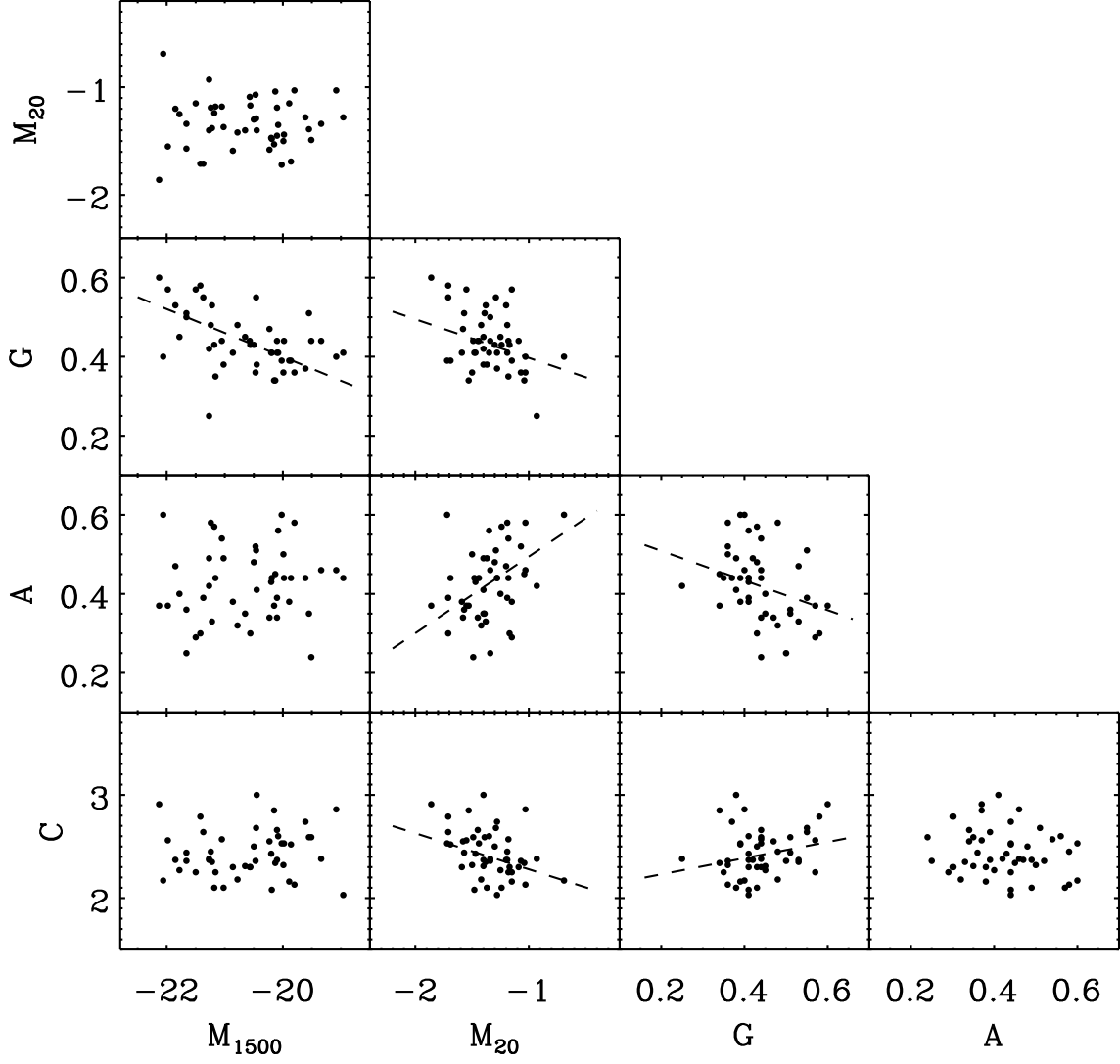
FIG. 3.— Correlations among C, A, G, M_{20}, and M_{1500} for the galaxies in our sample. Each parameter is correlated with one or more of the other parameters. There are also several strong relations among them. The dashed lines are the best linear fits to the relations. We see all expected correlations among these parameters, suggesting that these parameters could be still applicable for $z \geq 6$ galaxies, if used with caution.
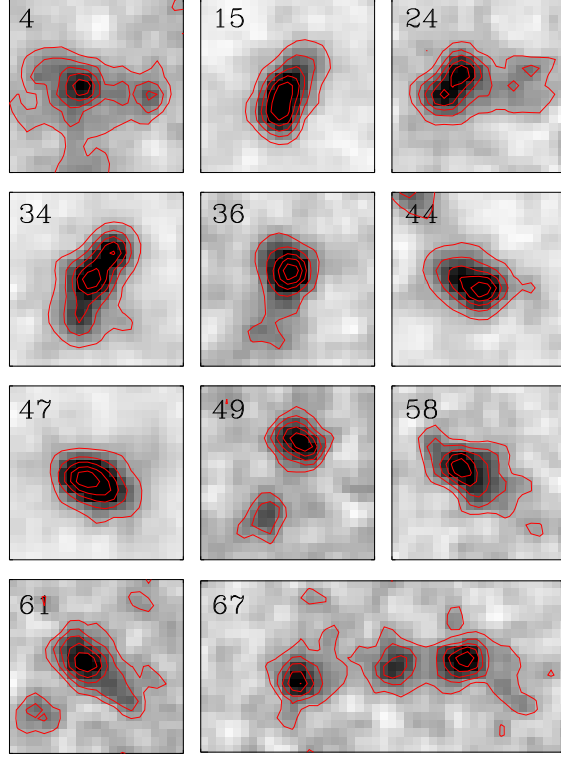
Fig. 4.— Interacting/merging galaxies in the HST images. The image size is $1''26 \times 1''26$. The red profiles are the contours of SB. Each contour starts at 85% of the peak value with an interval of 20%. These galaxies have extended and elongated features, and/or have double or multiple components.
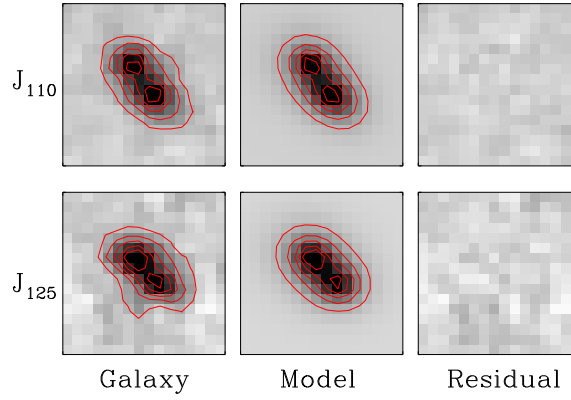
Fig. 5.— Images of the $z = 6.96$ LAE (no. 62). The two left-most images show the galaxy in the two J bands (J_{110} and J_{125}). The two images in the middle are the best-fit model (two Sérsic functions for the two components) galaxies. The residuals are on the right-hand side. The separation between the two components is about $0''2$ (~ 1 kpc).
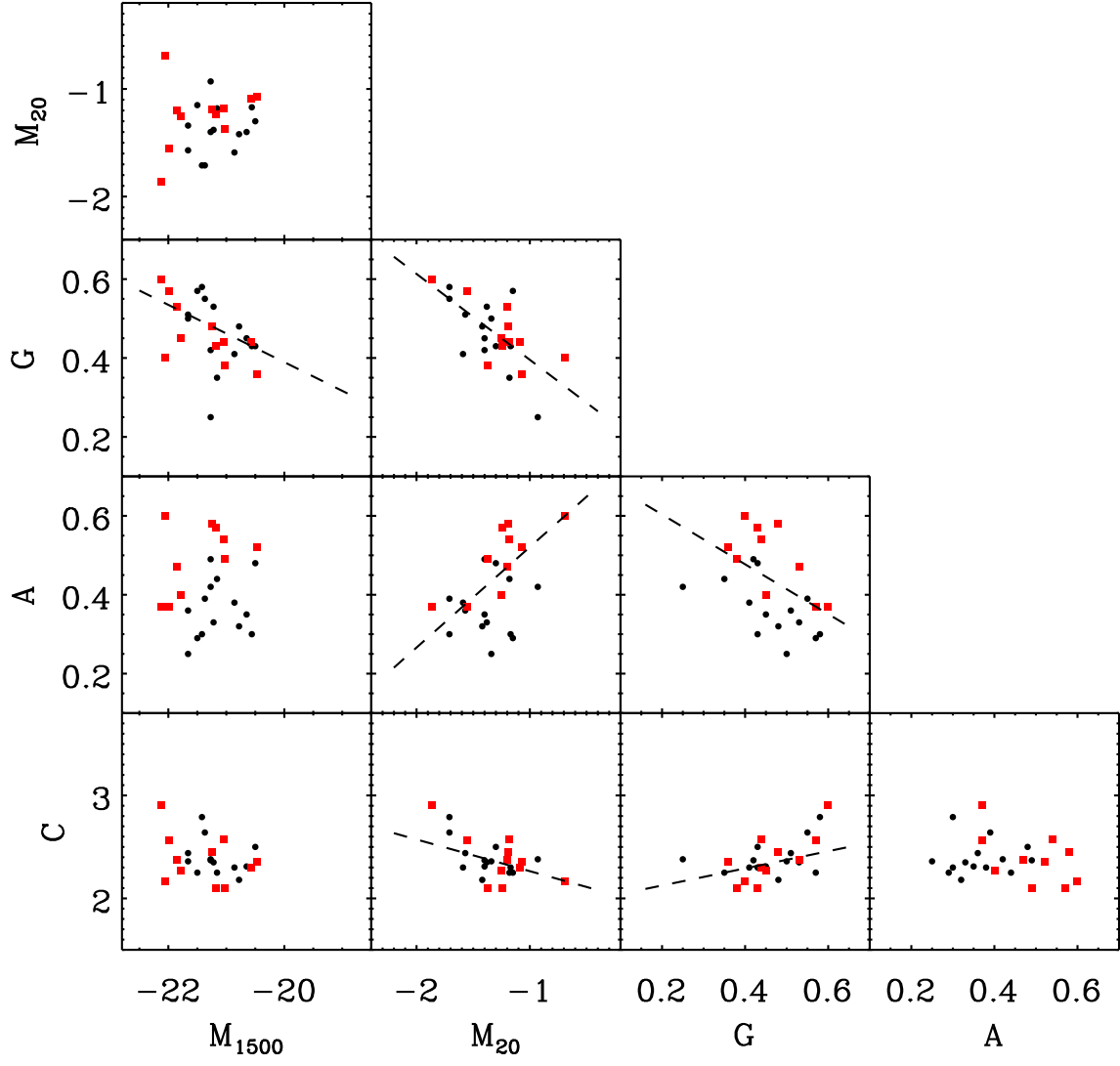
FIG. 6.— Same as Figure 4, but for galaxies with $M_{1500} \leq -20.5$ mag. The red squares represent the interacting galaxies identified in our sample. The figure also shows better corrections (smaller scatter) among the parameters compared to Figure 4.
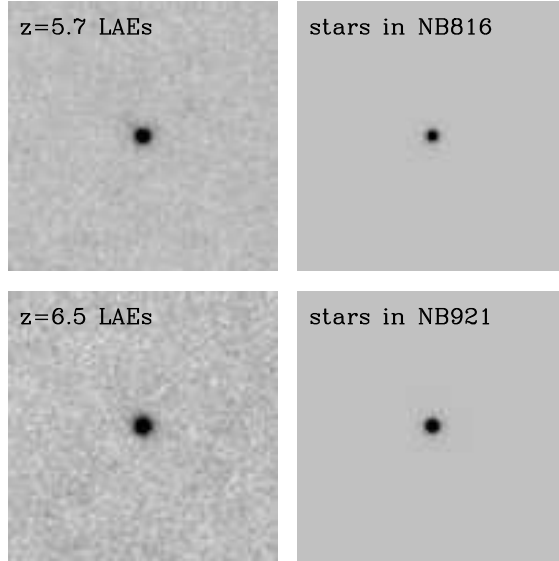
Fig. 7.— Stacked narrow-band images for LAEs and stars (or point sources) in two bands NB816 and NB921. The image size is $20'' \times 20''$. The images have the same intensity scale. The PSF FWHM sizes derived from the two stacked stars are $0\!''\!.49$ and $0\!''\!.61$, respectively. The FWHM of the stacked LAEs are $0\!''\!.61$ and $0\!''\!.77$, respectively. They are larger than the PSF sizes by 26%, because LAEs are not point sources. The stacked LAEs do not show diffuse Lyα halos.
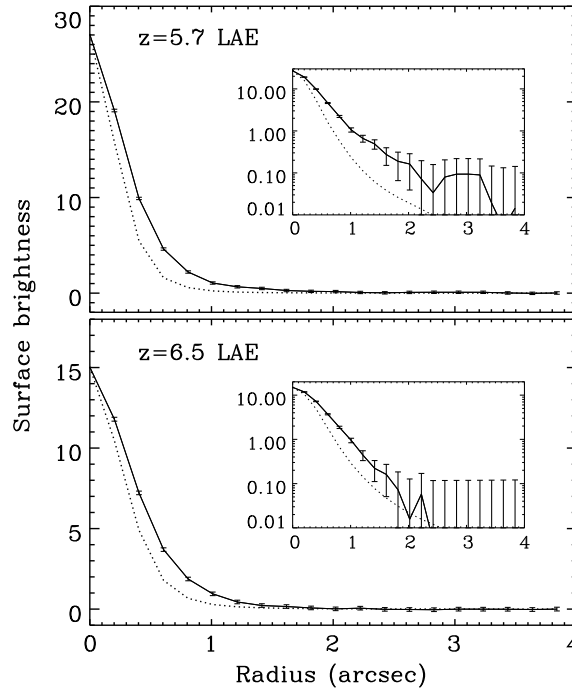

Fig. 8.— Radial profiles of the stacked images in Figure 7. The units of SB is 10^{-19} erg s^{-1} cm^{-2} arcsec^{-2}. The solid profiles with 1σ error bars represent the stacked LAEs, and the dashed profiles represent the stacked stars. The insets show the radial profiles on a log scale. The LAE profiles are broader than the PSF sizes, and exhibit slightly longer tails than the PSF profiles do, meaning that the Lyα emission is resolved. This is because galaxies are not point sources, as explained in Section 4.1. At $r \geq 2''$, the SB in both cases is consistent with zero within 1σ errors. We do not see very extended halos of Lyα emission.

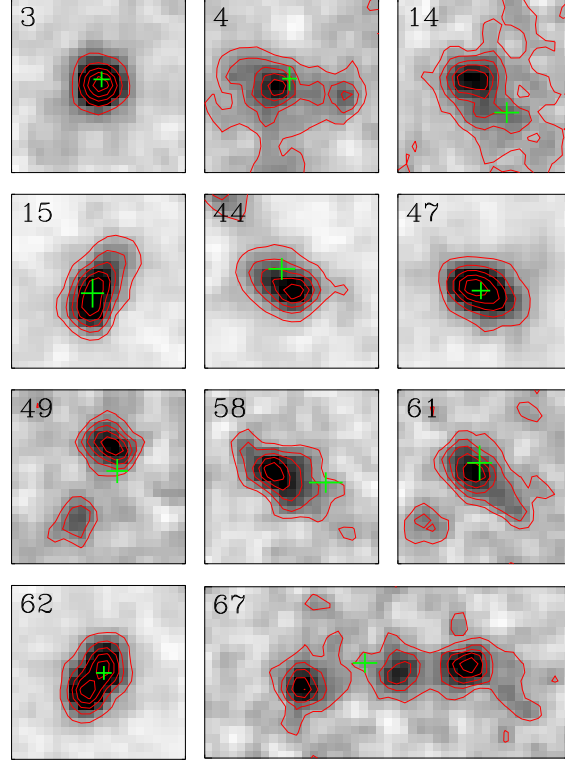FIG. 9.— Positions of UV continuum and Lyα emission for a sample of bright galaxies. The red contours and their scales are similar to those shown in Figure 4. They display the UV continuum emission seen in the HST images. The green crosses indicate the positions (and 1σ uncertainties) of the Lyα emission from our ground-based narrow-band images. The first object no. 3 represents a typical compact galaxy, whose positions of UV continuum and Lyα emission agree with each other. The rest of the objects are merging/interacting systems, which show a variety of Lyα position offsets relative to the UV continuum positions, including significant positional misalignment.